A new insight into hydrogen leakage phenomena: Visibly observable patterns of hydrogen leakage

Luqiao Yao,[1] Jianwei Li,[1,2,*] Qingqing Yang,[1] and Zhonghao Tian[1]
*Correspondence: jianwei.li@ieee.org

Received: January 22, 2026; Accepted: April 22, 2026; Published Online: April 23, 2026; https://doi.org/10.59717/j.xinn-energy.2026.100148

GRAPHICAL ABSTRACT

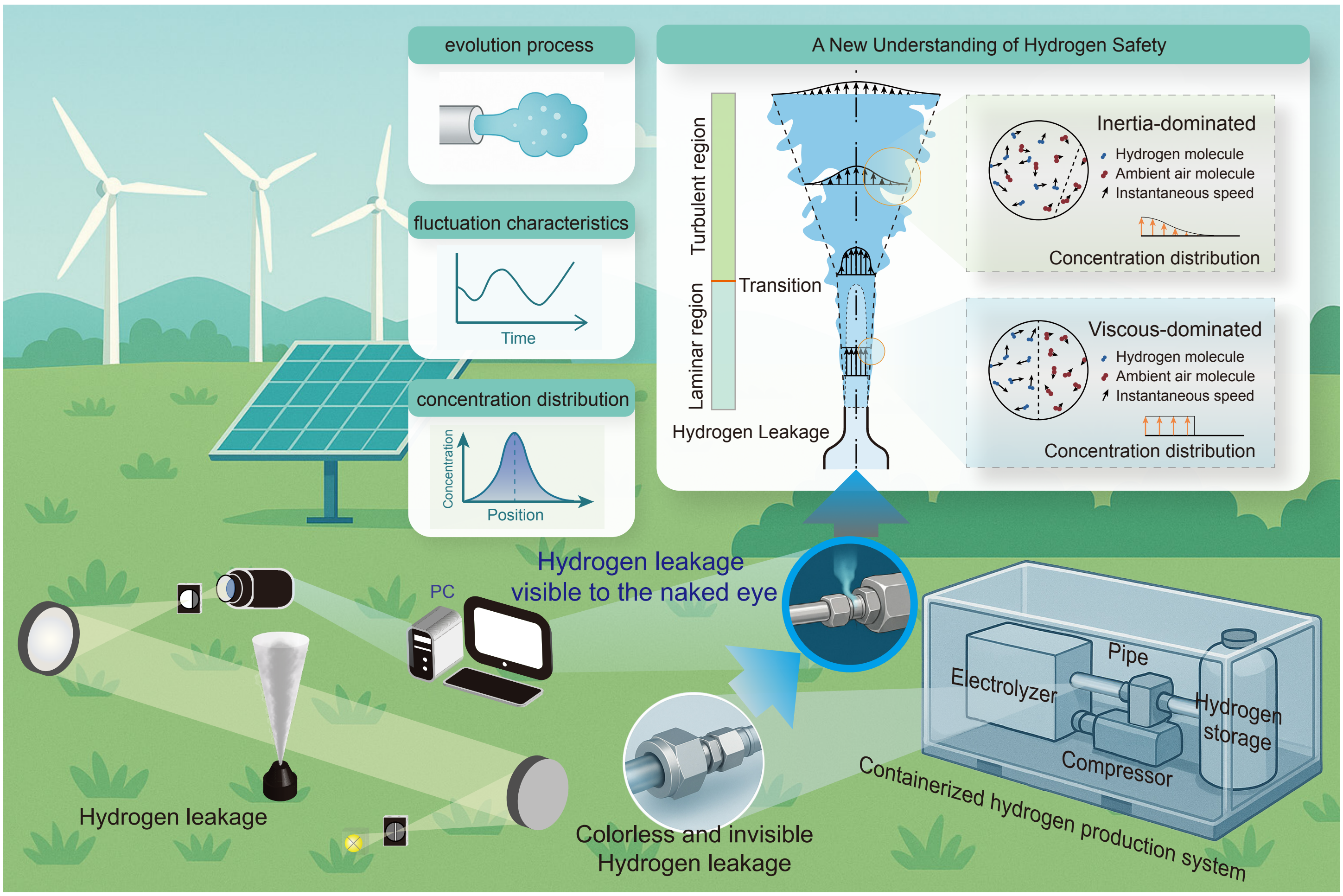

PUBLIC SUMMARY

- Flow characteristics of hydrogen leakage become visually observable.
- Key transition dynamics are revealed through visualization.
- Full-field concentration is constructed based on observed transition dynamics
- A new insight and visual confirmation of hydrogen leakage patterns is presented.

A new insight into hydrogen leakage phenomena: Visibly observable patterns of hydrogen leakage

Luqiao Yao,[1] Jianwei Li,[1,2,*] Qingqing Yang,[1] and Zhonghao Tian[1]
[1]School of Mechanical Engineering, Beijing Institute of Technology, Beijing, 100081, China
[2]Beijing Institute of Technology Zhuhai, Guangdong, 519088, China
*Correspondence: jianwei.li@ieee.org
Received: January 22, 2026; Accepted: April 22, 2026; Published Online: April 23, 2026; https://doi.org/10.59717/j.xinn-energy.2026.100148

Citation: Yao L., Li J., Yang Q., et al. (2026). A new insight into hydrogen leakage phenomena: Visibly observable patterns of hydrogen leakage. *The Innovation Energy* **3**:100148.

As hydrogen energy systems move toward miniaturization and modularization, the low-pressure, low-flow hydrogen leakage problem, which is becoming more frequent and significantly harder to detect, leading to the formation of flammable or explosive hydrogen-air mixtures, is a key challenge, constraining the widespread deployment of hydrogen technologies. The concentration distribution directly determines the extent and severity of flammable zones, but its spatiotemporal evolution, governed by the laminar-to-turbulent transition of the leakage jet, remains elusive. In this study, a visualization method is employed to observe hydrogen leakage, enabling the first clear depiction of the transition point's behavior in low-pressure hydrogen jets. The transition point is found to exhibit a dual nature, with a relatively certain average position accompanied by distinct spatial fluctuations. A full-field concentration distribution of hydrogen leakage is constructed based on the spatial characteristics and fluctuation patterns of the transition point, enabling an accurate description of the spatiotemporal variation in hydrogen concentration fields. This work provides new insight and visual confirmation of hydrogen leakage behavior, offering essential support for the transition of hydrogen's societal role—from a hazardous chemical to a safe and manageable energy carrier.

INTRODUCTION

With the growing global demand for clean energy, hydrogen has emerged as a promising energy carrier due to its zero carbon emissions, high energy density, and broad applicability.[1,2] It plays a critical role in addressing climate change, achieving carbon neutrality, enhancing energy security, and enabling green industrial transformation, and is widely regarded as a cornerstone of future energy systems.[3-4] As of 2024, more than 130 countries have incorporated hydrogen into their national energy strategies,[5] and hydrogen development has become a global consensus.[6]

Safety remains the fundamental prerequisite for the large-scale deployment of hydrogen energy.[7] Hydrogen is colorless and odorless, with an extremely low ignition energy and a wide flammability range (4%–75%),[8] making it highly susceptible to ignition or explosion in the event of leakage. Statistics indicate that among 576 recorded hydrogen-related incidents, approximately 79% involved ignition following leakage, and nearly half resulted in explosions.[9] Consequently, hydrogen leakage represents one of the most frequent and hazardous causes of hydrogen-related accidents.[10] In practical scenarios, weak points such as seals, valves, and pipelines are susceptible to microcracks or seal failures. Such leaks are often difficult to detect, with complex diffusion paths and poorly understood evolution, posing significant challenges for safety management.[11,12]

With the advancement of hydrogen systems toward miniaturization and modularization, hydrogen leakage is increasingly characterized by low pressure and low flow rates.[13-15] Unlike traditional high-pressure, large-flow leaks that exhibit strong turbulence, unsteady behavior, and directional jets,[16,17] low-pressure hydrogen leakage displays multi-scale, non-stationary flow characteristics.[18,19] In laminar regimes, hydrogen tends to diffuse along relatively stable paths with limited mixing, promoting the formation of high-concentration zones.[20] If such regions reach flammable limits and encounter ignition sources, severe explosions may occur. In contrast, turbulent mixing produces more intermittent and spatially dispersed concentration fields, increasing the uncertainty of hazardous regions.[21]

A key feature of low-pressure hydrogen jets is the laminar–turbulent transition.[22] The emergence of a transition point significantly alters the hydrogen diffusion rate and direction, thereby reshaping the spatial concentration distribution and the extent of the flammable region.[23] However, existing studies primarily focus on overall jet morphology or turbulence development,[24,25] while most leakage models rely on numerical simulations or empirical correlations.[26-28] Although the presence of transition points has been noted,[29,30] their formation mechanisms and spatiotemporal dynamics remain insufficiently characterized experimentally.

Present hydrogen detection methods are primarily based on traditional sensors, which are point-based and often intrusive.[31,32] Their accuracy is highly dependent on sensor placement, calibration, and response time, making them inadequate for capturing the global behavior of a leaking gas plume.[33,34] These limitations hinder effective identification of leakage paths and the boundaries of flammable zones in complex environments.[35]

In this study, a non-intrusive visualization method based on the unique physical and optical properties of hydrogen is proposed. No external tracers or reactive agents are required, and real-time observation of hydrogen leakage behavior is enabled. The formation, spatial evolution, and fluctuation characteristics of the transition point in low-pressure hydrogen jets are systematically investigated. The transition point is identified as a key flow structure, and its dominant influence on the resulting hydrogen concentration field is clarified. Based on these insights, a more comprehensive model of hydrogen concentration distribution is constructed. This work is intended to offer a novel perspective for understanding hydrogen dispersion under low-pressure, low-flow conditions and to provide theoretical and technical support for the safe design and risk management of future compact hydrogen energy systems.

MATERIALS AND METHODS

The experiment involved the visualization and detection of hydrogen leakage jets with varying initial flow rates and concentrations. As shown in Figure S1A, the setup includes a gas generation system, a Z-type high-speed Schlieren system, and an image acquisition system. Detailed experimental parameters are provided in Table S1. The gas generation system was used to produce hydrogen jets at specified flow rates, while the Z-type high-speed Schlieren system enabled high-frame-rate, high-resolution visualization of the hydrogen leakage jets. In the image acquisition system, NI-9203 and NI-9264 were used for signal input and output, with control handled via NI-DAQ. A LabVIEW-based upper computer was used to remotely control the on/off status of the gas circuit system and to display real-time and historical data from pressure, temperature, and flow sensors.

To ensure experimental safety and isolate the physical dispersion behavior of hydrogen, nitrogen was used as the background gas in all mixtures (20% to 100% vol.%) (Figure S1C). The experiment was conducted outdoors. An experimental setup with a top ventilation opening was constructed to ensure safety during hydrogen-related tests. One side of the setup included a door to allow for personnel and equipment access (Figure S1B).

For safety, the hydrogen jet pressure was remotely controlled using the upper computer, and Schlieren images were captured remotely. A total of 81 experimental conditions were established, with flow rates ranging from 2 to 10 SLM and hydrogen volume fractions from 20% to 100%.

Detailed methods are included in the supplemental information.

RESULTS AND DISCUSSION

Multistage evolution characteristics of hydrogen leakage jets

The flow pattern evolutions of 100% concentration hydrogen leakage jets (HLJ) under various outlet flow rates were explored by high-frequency (3000

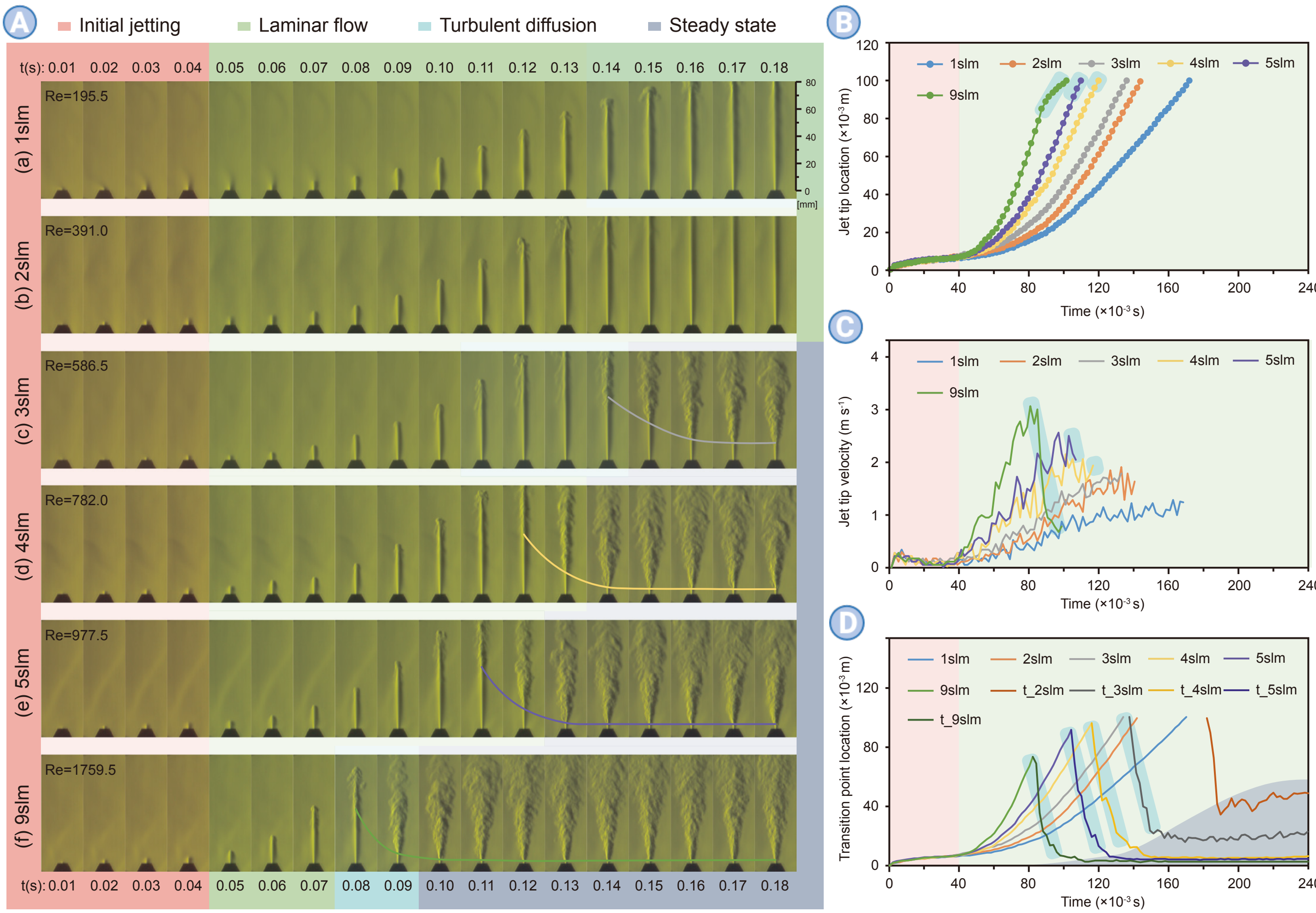

Figure 1. Time-resolved Schlieren images depicting different jet evolution modes (A) Visualization of time-domain images. (B) Jet tip position. (C) Axial propagation velocity. (D) Transition point position.

fps) Schlieren imaging. Each condition was repeated five times independently to ensure reproducibility, with a positional error of ± 0.1 mm. Experiments were conducted at an ambient temperature of 299.65K and light breeze conditions (Beaufort scale 1), with enclosures and thermal barriers set up to minimize external disturbances (Supplemental Figure S1, Supplemental Table S1).

At the initial stage, the HLJ exhibited a cylindrical laminar jet structure. As the flow developed, a transition to turbulence occurred at a certain height, after which the jet gradually evolved into a conical turbulent region. Ultimately, a dual-region structure formed, consisting of a cylindrical laminar core and a conical turbulent front. Based on representative time-resolved Schlieren image sequences (Figure 1A; one frame selected every 30 images), the jet evolution process can be divided into four distinct stages:

Stage I: Initial Jetting (red area)

Stage II: Viscosity-Dominated Stable Laminar Flow (green area)

Stage III: Turbulent Diffusion Triggered by Transition (blue area)

Stage IV: Steady-State Laminar–Turbulent Coexistence Region (purple area).

In Stage I (0.01–0.04 s), the leading edge of the jet exhibited a parabolic-like expansion across all flow rates. Governed by outlet velocity, jet momentum, and ambient conditions, the jets displayed a nearly uniform propagation trend. No significant instabilities were observed at this stage.

During Stage II, the HLJ front remained smooth and symmetric, indicating a flow field still dominated by viscous effects. Shear-layer disturbances were weak, Reynolds numbers remained low, and no pronounced fluctuations were observed. The diffusion rate varied with flow rate, resulting in distinct spreading behaviors (Figure 1A-C).

As time progressed, increasing velocity gradients within the shear layer triggered Kelvin–Helmholtz (K–H) instabilities, marking the onset of Stage III. This stage was characterized by the formation and subsequent breakdown of primary vortices into vortex rings, generating axisymmetric distorted structures that appeared as "mushroom-shaped" features at the jet front. Vortex energy accumulated along the axial direction, elevating local Reynolds numbers to critical levels and causing the transition point to migrate downstream toward the nozzle (Figure 1A&D). As the transition developed, the turbulent region progressively engulfed portions of the upstream laminar region. This process occurred rapidly, typically within three image frames.

Figure 1D reveals a strong negative correlation between the transition onset time and its final steady-state position across different flow rates. At higher flow rates, steeper velocity gradients in the shear layer accelerated instability development, leading to earlier transition onset and transition points located closer to the nozzle. Conversely, at lower flow rates, disturbances developed more gradually, resulting in delayed transitions occurring farther downstream.

Notably, the migration of the transition point was not synchronized with the overall jet front propagation. For $Q \geq 5$ SLM, the transition point exhibited a clear downward shift within the observable region. However, under low flow rate conditions (Q= 1, 2 SLM), the transition point remained outside the visible range, indicating limited turbulence development and predominantly laminar jet behavior. Specifically, for Q= 9 SLM, a distinct transition occurred at the jet tip (71 mm) at t = 0.08 s, followed by rapid migration upstream toward the nozzle. This turbulent expansion decelerated the jet's axial growth (Figure 1B&D).

Ultimately, all high-flow HLJs developed a relatively steady dual-region structure, comprising a turbulence-dominated front region characterized by dominant vortices and a viscous laminar tail maintaining approximate

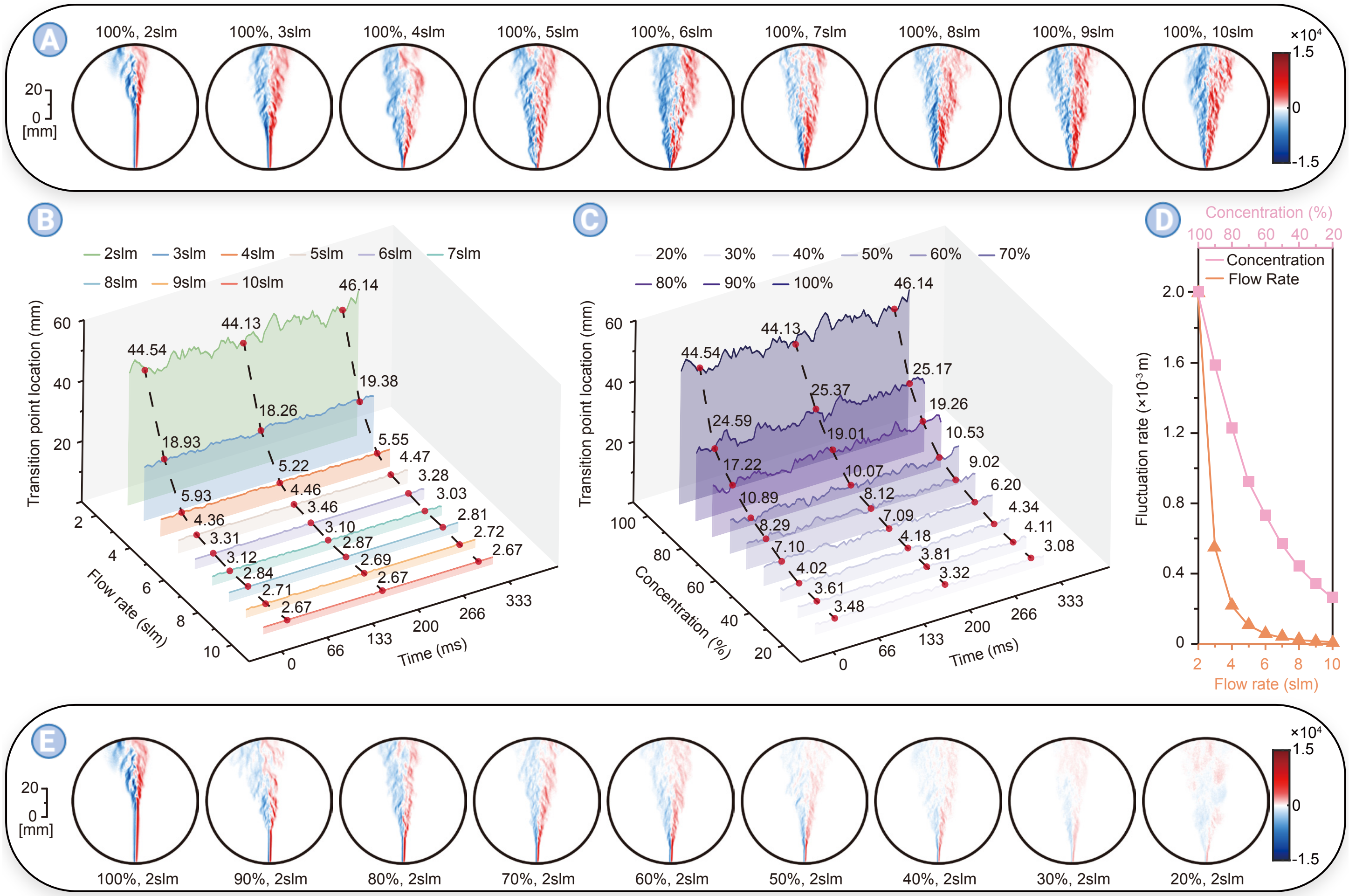

Figure 2. Fluctuation characteristics of the laminar–turbulent boundary in HLJs (A) Time-resolved Schlieren grayscale images under Q = 2–10 SLM (C =100 vol.% hydrogen). (B) Time series of dual-region boundary height Q = 2–10 SLM, C =100 vol.% hydrogen). (C) Time series of boundary height at Q = 2 SLM with C =20–100 vol.% hydrogen. (D) Quantified fluctuation. (E) Time-resolved Schlieren grayscale images under Q =2 SLM with C =20–100 vol.% hydrogen.

symmetry. The formation of this structure marked the classical dual-region pattern of shear-driven jets (Stage IV).

The transition from Stage III to Stage IV was determined based on a combined temporal–statistical–morphological criterion. Specifically, the flow is considered to reach a quasi-steady state when: (i) the transition point height $h(t)$ shows no systematic drift over a time window of at least 0.01 s; (ii) the standard deviation of $h(t)$, evaluated over a moving window, exhibits convergence with relative variation within ±5%; and (iii) the overall jet morphology, characterized by a stable laminar core and turbulent front, remains invariant without further large-scale structural evolution. The onset of Stage IV is defined as the earliest time at which these conditions are simultaneously satisfied.

To further assess the role of buoyancy, the Richardson number was estimated as

$$R_i = g\left(\rho_a - \rho_j\right)/\rho_a \cdot D/U^2 \qquad (1)$$

where g is the gravitational acceleration, ρ_a and ρ_j are the densities of ambient air and hydrogen, respectively, D is the nozzle diameter, and U is the jet exit velocity.

Under the present experimental conditions (Q=2–10SLM， C=20–100 vol.% hydrogen), the calculated values of R_i range from 10^{-8} to 10^{-4}, indicating a momentum-dominated regime ($R_i \ll 1$). Therefore, the transition dynamics in the third and fourth stages are primarily governed by shear-layer instabilities induced by velocity gradients, while buoyancy plays only a secondary role.

Fluctuation characteristics of the laminar–turbulent boundary

After reaching a quasi-steady state, the laminar–turbulent boundary height of the HLJ—that is, the transition point position—exhibited noticeable temporal fluctuations. The stability of this boundary was significantly influenced by the jet's initial flow rate and hydrogen concentration.

Figure 2A&E present time-resolved Schlieren grayscale images under typical conditions:

Varying flow rates (Q= 2–10 SLM, C=100 vol.% hydrogen), and

Varying concentrations (Q= 2 SLM, C=20–100 vol.% hydrogen).

The results show that, under all tested conditions, HLJs developed a characteristic dual-region structure, with coexisting laminar and turbulent flow zones.

To quantify the fluctuation of the transition point, 1000 images were captured at a frame rate of 3000 fps, and the transition point position was extracted every 10 frames for time-series analysis. Each experimental condition was repeated five times independently, yielding an average relative error of 3.2% and a reproducibility index (ICC) of 0.91.

Figure 2B&C show the time series of the transition point height under typical conditions (Q= 2–10 SLM, C=100 vol.% hydrogen; Q= 2 SLM, C=20–100 vol.% hydrogen).

Theoretically, the initial momentum flux of the jet can be approximated by

$$J = \int_A \rho u^2 dA \qquad (2)$$

where ρ is the jet density, u is the outlet velocity distribution, and A is the nozzle outlet area.

As the flow rate increases, both the jet exit velocity and momentum flux rise, strengthening inertia-dominated behavior. In the shear layer, high-momentum jets exhibit greater resistance to external disturbances. Specifically, enhanced shear stress accelerates the formation and stabilization of coherent vortical structures, which suppresses the growth of Kelvin–Helmholtz (K–H) instabilities and consequently reduces fluctuations in the transition point.

Additionally, higher flow rates increase the characteristic Reynolds number (Re), promoting convective dominance in the flow, which contributes to a more stable and well-defined turbulent region.

On the other hand, variations in gas concentration influence jet stability indirectly via density gradients. Higher hydrogen concentrations reduce the mixture density and increase the magnitude of $\nabla\rho$, which enhances buoyancy-related perturbations within the shear layer. These effects promote the growth of K–H instabilities, facilitate the penetration of turbulence into the laminar region, and increase the temporal variability of the transition point height.

To quantify the influence of flow rate and concentration on boundary stability, the standard deviation of the transition point position is used as a metric, and its variation with flow rate and concentration is presented in Figure 2D. The experimental results show that for pure hydrogen leakage, increasing the flow rate from 2 SLM to 10 SLM reduces the fluctuation amplitude of the boundary by approximately 99.44%. In comparison, decreasing the hydrogen concentration from 100 vol.% to 20 vol.% leads to a reduction of about 87.08%. These results indicate that flow rate variations directly suppress boundary disturbances by enhancing momentum transport, whereas concentration effects act indirectly through density gradients and therefore have a relatively weaker influence.

In summary, the steady-state fluctuation behavior of the HLJ boundary reflects a competition between enhanced momentum flux and density-gradient-induced disturbances. High flow rates promote boundary stability, while high hydrogen concentrations tend to increase fluctuations. The overall stability of the HLJ flow field is therefore governed by the combined effects of these two factors.

Transition point fluctuation analysis

Under low-pressure and low-flow conditions, the axial transition position of pure hydrogen jets, denoted as $h(t)$, exhibits significant non-stationary fluctuations and shows high sensitivity to perturbations. Experimental observations reveal that these fluctuations are neither purely random walks nor clearly periodic but instead represent a mean-reverting process that gradually returns to an equilibrium position after deviation.

This behavior arises from the interaction between shear-layer velocity gradients and evolving turbulent structures. When the transition point deviates from its equilibrium position h^*, the instability of the shear layer increases, generating a restoring tendency that drives the system back toward equilibrium. This restoring force can be analogized to a linear elastic force, with its intensity proportional to the displacement $h'(t) = h(t) - h^*$, expressed as:

$$F_r \propto -\gamma h'(t) \tag{3}$$

Meanwhile, viscous dissipation from turbulence suppresses the growth of this deviation, described by:

$$F_d \propto -\rho v_t \frac{dh'(t)}{dt} \tag{4}$$

Together, these mechanisms govern the transition point's fluctuation dynamics, which can be approximately modeled as a one-dimensional Ornstein–Uhlenbeck (OU) process:

$$dh'(t) = -\gamma h'(t)dt + \sigma dW(t) \tag{5}$$

where $h'(t)$ denotes the fluctuation of the transition point position from its mean value, γ is the restoring coefficient representing the rate of return toward equilibrium (a measure of system "rigidity" or stability strength), σ is the fluctuation amplitude (external disturbances), and $dW(t)$ denotes a Wiener process.

To validate the OU process assumption, transition point time series $h(t)$ were extracted from 81 experimental conditions, covering flow rates Q= 2–10 SLM and volume fractions C=20–100 vol.% H_2. The transition point was identified based on the geometric characteristics of iso-grayscale contours extracted from Schlieren images. A consistent grayscale threshold was used to define the jet boundary. In the laminar region, contours remain nearly parallel to the jet axis, whereas in the turbulent region, enhanced mixing produces inclined contours with a distinct spreading angle. The transition point is defined as the inflection point where the contour orientation changes from near-vertical to inclined.

After detrending via moving average, the fluctuation components $h'(t)$ were obtained. Statistical tests including the Augmented Dickey–Fuller (ADF, average $p < 0.05$) and KPSS tests (average $p > 0.1$) support stationarity. Autocorrelation analyses show strong ACF/PACF correlation at lag 1 followed by exponential decay. Power spectral density is concentrated in the low-frequency range with no sharp peaks (Supplemental Figure S2, S3, S4). These features are consistent with the mean-reverting behavior expected of an OU process. Furthermore, ARIMA fitting results showed all samples conforming to an AR(1,0,0) model, further supporting the suitability of OU modeling.

Maximum likelihood estimation (MLE) was used to extract OU parameters γ and σ under various flow rates and concentrations. Residuals passed Ljung–Box tests for autocorrelation and Shapiro–Wilk tests for normality, confirming the statistical robustness of the fitting.

Empirical mappings were then established between the OU model parameters and experimental variables Q(flow rate) and C(concentration): (Figure 3A&B)

$$\gamma \approx 2.265 \cdot 10^{4} \cdot Q^{0.471} \cdot \exp(-0.537 \cdot C),$$
$$\sigma \approx 3.114 \cdot 10^{-20} \cdot Q^{-3.103} \cdot \exp(2.417 \cdot C) \tag{6}$$

Here, the flow rate Q has been converted from standard liters per minute (SLM) to cubic meters per second (m^3/s).

The restoring coefficient γ reflects the rate at which the transition point returns to its equilibrium position and is closely related to the stability of the shear layer. As the flow rate increases, both the jet exit velocity and the velocity gradient in the shear layer become larger, strengthening the self-recovery mechanisms associated with shear-driven instabilities, thereby increasing γ. In contrast, increasing the hydrogen concentration reduces the mixture density and enhances the density gradient relative to the ambient air. Due to intensified mass diffusion and viscous dissipation, coherent shear-layer structures are weakened, leading to a reduction in the effective restoring strength and thus a decrease in γ.

The fluctuation intensity σ reflects the combined effects of disturbance growth and dissipation. Higher flow rates generally suppress random fluctuations, whereas concentration-dependent diffusion modulates their amplitude. As a result, σ increases with increasing hydrogen concentration.

Model predictions across the full dataset yielded a root mean square error (RMSE) of 13.81 and a mean absolute percentage error (MAPE) of 5.15% for γ, and RMSE of $3.51 \cdot 10^{-7}$ and MAPE of 2.41% for σ, indicating strong explanatory capability both statistically and physically.

The explicit solution of the OU model is:

$$h'(t) = h'(0)e^{-\gamma t} + \sigma \int_0^t e^{-\gamma(t-\epsilon)} dW(s) \tag{7}$$

To further analyze the statistical behavior of the dual-region boundary height, transition point heights were extracted under 81 experimental conditions with flow rates Q= 2–10 SLM and volume fractions C=20–100 vol.% hydrogen. Each condition was repeated five times, and the extraction error was controlled within ±0.1 mm. Results showed that all free jets exhibited a typical dual-region structure with a near-nozzle laminar core and a far-field turbulent front.

In turbulent shear layers, quantities such as structural noise and energy spectra often scale with momentum flux via power laws. Unlike the fluctuation intensity σ, which characterizes the system's dynamic response to perturbations, the mean transition height h^* better reflects the global structural evolution of the jet. To quantitatively describe how h^* varies with flow rate and concentration, the following empirical model is proposed:

$$h^* = H_\infty + H \cdot \exp(-k_Q \cdot Q) \cdot \exp(-k_C \cdot C) \tag{8}$$

where H_∞ represents the minimum transition height under the high-flow, low-concentration limit, reflecting the rapid onset of turbulence near the nozzle

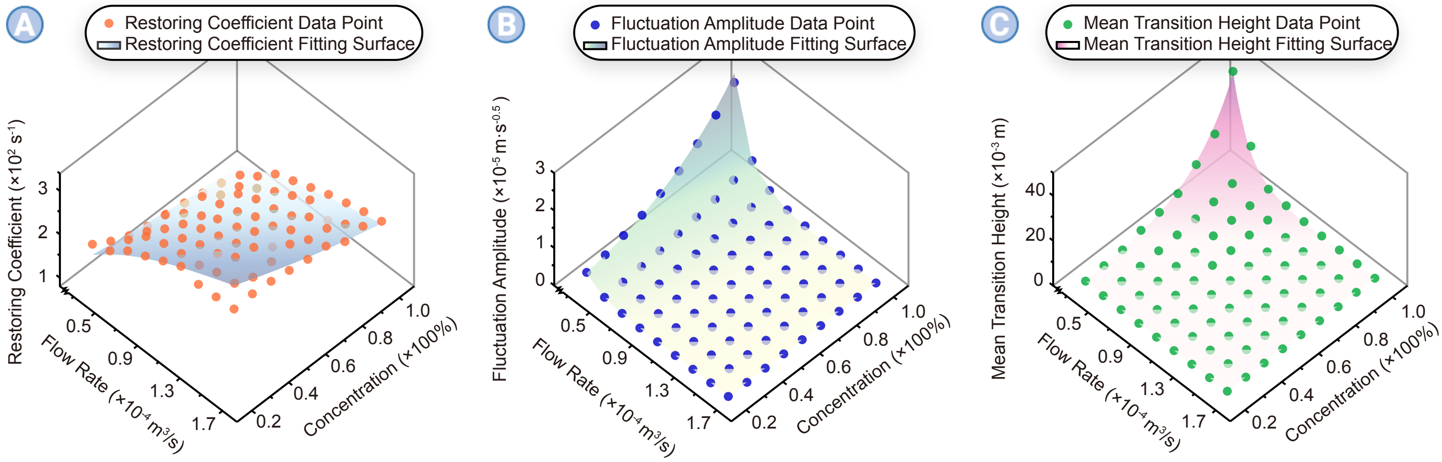

Figure 3. Analysis of laminar–turbulent boundary fluctuations (A) Restoring coefficient. (B) Fluctuation amplitude. (C) Mean Boundary Height. (All under 81 experimental conditions with Q= 2–10 SLM, C=20–100 vol.% hydrogen)

due to intense shear, H denotes the additional elevation of the transition point under low-flow, low-concentration conditions, k_Q and k_C characterize the effects of flow-induced instability and concentration-enhanced mass diffusion, respectively.

Experimental results show that increasing flow rate Q enhances jet momentum and shear-layer gradients, accelerating instability growth and shifting the transition point closer to the nozzle, following an exponential decay toward H_∞. In contrast, increasing hydrogen concentration C enhances mass diffusion and reduces effective shear, delaying instability onset and elevating the mean transition height. Additional dissipation at high concentrations further suppresses disturbance growth.

The fitted empirical model is: (Figure 3C)

$$h^* = 2.699\cdot 10^{-3}\cdot \exp(-6.767\cdot 10^4\cdot Q)\cdot \exp(5.029\cdot C) + 2.277 (R^2 = 0.986) \quad (9)$$

with RMSE = 0.688 and MAPE = 4.53%.

Full-field concentration construction

Under the present low-pressure conditions, the Joule–Thomson coefficient of hydrogen near ambient temperature is sufficiently small that the associated temperature changes during expansion can be neglected. The experiments were performed in a controlled environment, with adequate separation between the light source and the test section, and no observable thermal plumes or background distortions unrelated to the jet were identified in the baseline images.

An image-processing-based grayscale-to-concentration conversion program was developed to calibrate Schlieren images and reconstruct the concentration field (Figure 4D) (Supplemental text). The resulting concentration contour map clearly demonstrates the rapid decay of jet concentration from the high-concentration near-nozzle region to the downstream turbulent mixing zone (Figure 4A-C). To minimize outlet-induced artifacts, the initial concentration was calibrated at 5 pixels downstream of the nozzle exit. The jet region was segmented based on grayscale gradients, followed by parameterization and fitting. Radial grayscale profiles at different axial locations were extracted to reconstruct the corresponding concentration fields.

For the axial concentration distribution of the HLJ, the axial decay of concentration in the near-field laminar region ($z \le z_{tr}$) can be derived based on mass conservation. Considering a cylindrical control volume along the jet centerline and neglecting axial diffusion, transport is advection-dominated, with molecular diffusion prevailing while momentum and turbulent mixing remain underdeveloped. Assuming constant axial velocity and a uniform radial mass loss rate, the axial concentration gradient becomes constant, leading to a linear decay in concentration (Figure 4E) (Supplemental Figure S5):

$$c_l(z) \approx c_0 - kz \approx 0.699 - 0.967\cdot z (R^2 \approx 0.965) \quad (10)$$

where c_0 is the initial concentration and k is the decay coefficient in the laminar region, implying $c_l(z) \propto z$.

In the transitional region ($z_{tr} < z \le z_t$), the jet evolves from laminar to turbulent as shear-layer instabilities generate large-scale vortices.

Although mixing is enhanced, the flow has not yet reached a fully developed self-similar turbulent state. Under these conditions, the axial concentration follows a convection–diffusion balance dominated by radial mixing, resulting in a power-law decay:

$$c_{t,1}(z) \approx mz^{-\alpha} \approx 0.074z^{-0.493} (R^2 \approx 0.979) \quad (11)$$

indicating $c_{t,1}(z) \propto z^{-0.493}$, where m is the initial decay rate and α is the intensity scale.

When the jet extends beyond approximately 7d axially, it fully transitions into a developed turbulent state with self-similar structure ($z > z_t$). Based on momentum conservation $\int_0^\infty \rho u^2 r dr = \text{const}$ and self-similarity theory, the concentration decays as:

$$c_{t,2}(z) \approx nz^{-1} \approx 9.375\times 10^{-3}\cdot z^{-1} (R^2 \approx 0.998) \quad (12)$$

Confirming the behavior of a classical turbulent free jet, consistent with theoretical predictions (George, 1989 [36]; Pope, 2000 [37]).

While the axial concentration profile describes the longitudinal dilution behavior, the radial distribution is used to characterize the transverse spreading of the jet. From the axisymmetric incompressible jet mass conservation equation:

$$\frac{\partial c}{\partial t} + u\frac{\partial c}{\partial z} + v\frac{\partial c}{\partial r} = D\left(\frac{1}{r}\frac{\partial}{\partial r}\left(r\frac{\partial c}{\partial r}\right) + \frac{\partial^2 c}{\partial z^2}\right) \quad (13)$$

assuming quasi-steady state ($\partial c/\partial t \approx 0$) and negligible axial diffusion, the system is dominated by radial diffusion. Assuming a self-similar form of the concentration field:

$$c(r,z) = c_z\cdot f(\eta), \eta = r/\sigma_z(z) \quad (14)$$

the radial concentration intensity is defined as:

$$A(z) = 2\pi\int_0^\infty c(r,z)\cdot r dr \quad (15)$$

Under the boundary condition $\left| r\frac{\partial c}{\partial r}\right|_0^\infty = 0$, the axial derivative simplifies to $\frac{dA}{dz} = 2\pi D\left[r\frac{\partial c}{\partial r}\right]_0^\infty = 0$. However, in reality, due to irreversible mixing and vortex transport, the effective mixing area expands, and $A(z)$ increases. Experimental observations lead to a segmented evolution model:

$$A(z) = \begin{cases} A_0 + k_{al}\cdot & z \quad z \le z_{tr} \\ A_\infty - \Delta A\cdot \exp(-k_{at}(z - z_{tr})) & z > z_{tr} \end{cases} \quad (16)$$

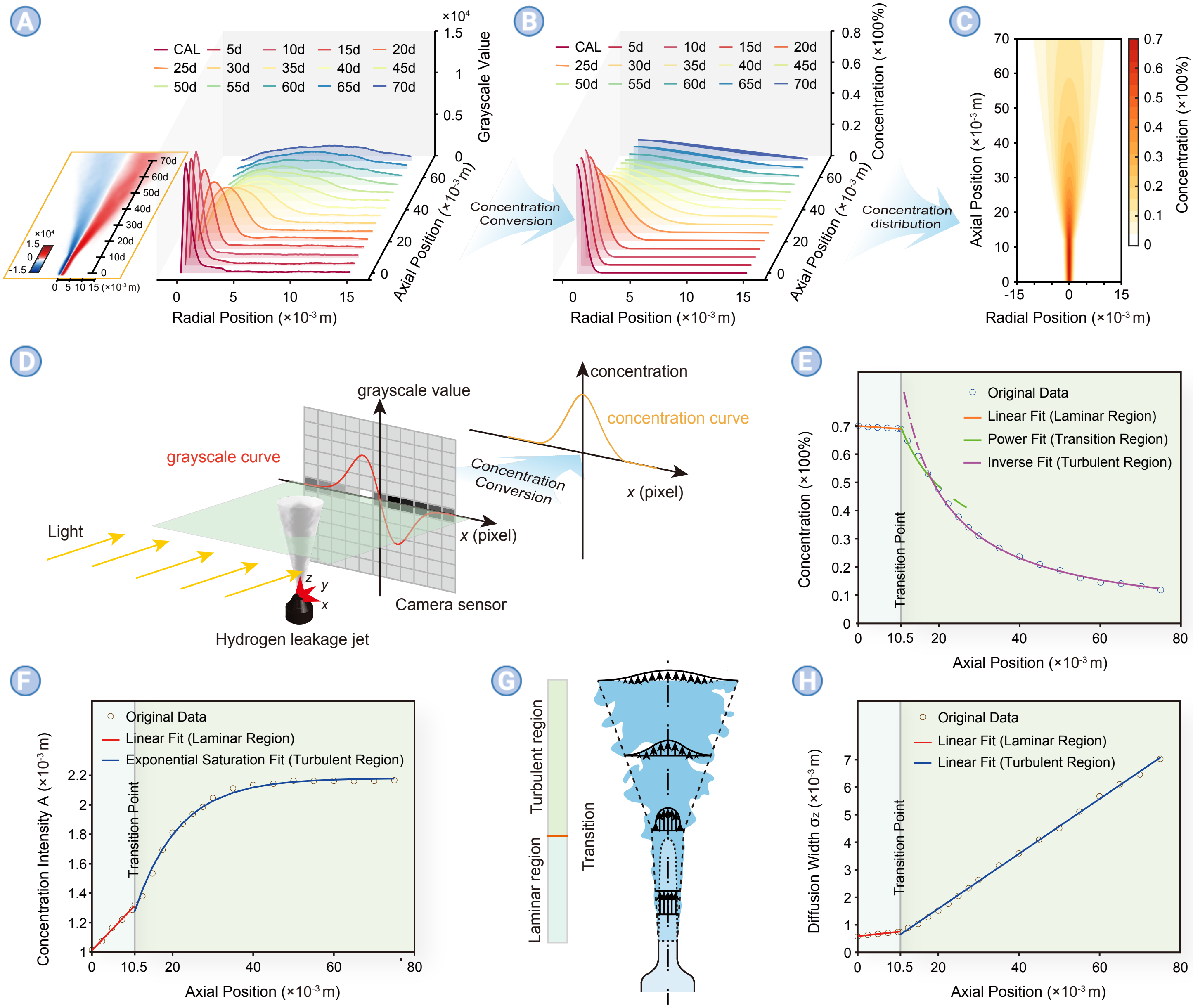

Figure 4. Reconstruction of the full-field concentration distribution (A) Grayscale difference contour map for 2 SLM and 70 vol.% case, along with radial grayscale difference profiles at different axial positions. (B) Radial concentration profiles. (C) Reconstructed concentration contour map. (D) Schematic of grayscale-to-concentration conversion. (E) Axial concentration distribution. (F) Radial concentration intensity. (G) Two-region jet structure. (H) Radial diffusion width.

where A_0 is the initial intensity, k_{al} is the laminar growth slope, z_{tr} is the transition height, $A_{tr} = A_0 + k_L \cdot z_{tr}$ is the intensity at the transition, $\Delta A = A_\infty - A_{tr}$ is the turbulent mixing gain, and A_∞ is the saturation value.

The radial diffusion width is defined as $\sigma_z^2(z) = \frac{\int_0^\infty c(r,z) r^3 dr}{\int_0^\infty c(r,z) r dr}$, also exhibiting a two-stage growth:

$$\sigma_z(z) = \begin{cases} \sigma_0 + k_{\sigma l} z & z \le z_{tr} \\ -\sigma_{tr} + k_{\sigma t}(z - z_{tr}) & z > z_{tr} \end{cases} \tag{17}$$

The radial distribution follows a Gaussian profile:

$$c(z,r) = \frac{A(z)}{\sigma_z(z)\sqrt{2\pi}} exp\left(-\frac{r^2}{2\sigma_z^2(z)}\right) \tag{18}$$

In the laminar region (Figure 4F):

$$A(z) = 28.709z + 1.011 \, (R^2 \approx 0.994) \tag{19}$$

indicating dominant axial transport and limited radial dilution (Figure 4H).

$$\sigma_z(z) = 15.823z + 0.587, (R^2 \approx 0.990) \tag{20}$$

The laminar region shows weak diffusion due to undeveloped shear instabilities. After transitioning, both $A(z)$ and $\sigma_z(z)$ exhibit slope discontinuities:

$$A(z) = 2.181 - 0.911 \cdot \mathbf{exp}(-91.103(z - z_{tr})) \, (R^2 \approx 0.994) \tag{21}$$

$$\sigma_z(z) = 99.664z - 0.407 (R^2 \approx 0.999) \tag{22}$$

indicating vortex-induced enhancement of radial momentum and mass diffusion. As the turbulent jet enters a quasi-self-similar regime, axial decay and radial diffusion reach dynamic balance, and both $A(z)$ and $\sigma_z(z)$ stabilize. Error analysis yields RMSE = 0.0182 and MAPE = 0.87% for $A(z)$, and RMSE = 0.0505 and MAPE = 1.90% for $\sigma_z(z)$.

The transition point height plays a decisive role in determining the concentration morphology and diffusion structure in HLJs. In real jets, the transition position is not fixed but fluctuates significantly, especially in the near field, reflecting the statistical nature of local instabilities and boundary layer development. Therefore, this work introduces an OU process to dynamically model the transition height $h(t)$:

$$dh(t) = \gamma(h^* - h)dt + \sigma dW(t) \tag{23}$$

Based on this, a time-coupled 3D concentration field model is constructed:

$$c(z,r,t) = \frac{A(z,t)}{\sigma_z(z,t)\sqrt{2\pi}} exp\left(-\frac{r^2}{2\sigma_z^2(z,t)}\right) \tag{24}$$

To more accurately reflect the influence mechanism of transition fluctuations in the actual concentration field, supplementary experimental analyses were conducted under representative conditions (Q= 2 SLM at 80%, 90%, and 100% vol., as well as 3, 4, and 5 SLM at 100% vol.) (Supplemental Figure S6, Supplemental Table S2, S3, S4). The results show that under all conditions, the axial concentration exhibits an approximately linear decay in the laminar region, with a consistent linear slope of 1.00 ± 0.20. In the transition region, the concentration decay still follows a power-law relationship, with the power exponent α stabilized in the range of -0.50 ± 0.025.

The length of the transition region depends on the local Reynolds number and disturbance propagation distance and follows an inverse power-law relationship with the transition height:

$$L_{tr}(c,q) = L_0 \cdot \left(\frac{h^{(0)}}{h(c,q)}\right)^a \tag{25}$$

where L_0 is the reference transition length, $h^{(0)}$ is the baseline transition height, and a is an empirical exponent, found to be approximately $a \approx 0.7$. In the turbulent region, the axial concentration decays approximately as an inverse first power, with exponent stabilized at -1.00.

Under varying experimental conditions, the radial concentration integral intensity $A(z)$ exhibits a consistent segmented evolution behavior. In the laminar region, $A(z)$ increases linearly and is expressed as:

$$A(z) = k_{al}z + A_0, k_{al} \approx 38.15c \tag{26}$$

In the turbulent region, $A(z) = A_\infty - \Delta A \cdot \exp(-k_{at}(z - z_{tr}))$. Higher concentrations and lower flow rates lead to larger values of both ΔA and A_∞, and smaller values of k_{at}.

The corresponding diffusion scale $\sigma_z(z)$ also shows a piecewise linear growth. In the laminar region:

$$\sigma_z(z) = k_{\sigma l}z + \sigma_0 \tag{27}$$

with $k_{\sigma l}$ nearly constant.

In the turbulent region:

$$\sigma_z(z) = k_{\sigma t}(z - z_{tr}) + \sigma_{tr} \tag{28}$$

where $k_{\sigma t} \approx 134.20c$

Overall, the experimental results are in strong agreement with the proposed segmented concentration model in both axial and radial directions, with discrepancies remaining within acceptable limits. These findings confirm the reliability and applicability of the proposed modeling framework.

CONCLUSION

In this study, hydrogen leakage phenomena under low-pressure and low-flow conditions were investigated through high-resolution flow visualization. The multi-stage evolution, laminar–turbulent transition mechanisms, and fluctuation dynamics of the transition point were systematically characterized. A flow structure specific to low-pressure, low-flow hydrogen leakage jets was identified, and the competing effects of flow rate and concentration on flow stability were quantitatively assessed.

It was demonstrated that the transition point exhibits statistically stationary, mean-reverting fluctuations, which were well described by an Ornstein–Uhlenbeck process. The typical fluctuation amplitude of the transition height was found to decrease by approximately 99.4% as the flow rate increased from 2 to 10 SLM, while a reduction of concentration from 100 to 20 vol.% led to an 87.1% decrease in boundary fluctuation intensity. The restoring coefficient increased monotonically with flow rate, whereas the fluctuation amplitude decreased with both increasing flow rate and concentration, indicating enhanced shear-induced stabilization and viscous dissipation at higher operating conditions.

Based on the spatial location and temporal fluctuation behavior of the transition point, the full-field concentration distribution was reconstructed. Quantitatively, the axial centerline concentration in the laminar region was shown to decay approximately linearly, with a characteristic slope on the order of -1.00 ± 0.20. In the transitional region, the concentration followed a power-law decay with a scaling exponent of −0.50 ± 0.025, while in the fully turbulent region the decay approached the classical turbulent jet scaling of −1.00. The radial integral concentration intensity exhibited a segmented evolution, increasing linearly in the laminar region and approaching exponential saturation in the turbulent regime, whereas the diffusion scale grew in a piecewise linear manner, with a significantly larger growth rate after transition.

These findings offer new experimental insights into the flow dynamics and mixing behavior of hydrogen under low-pressure, low-flow conditions. They also provide a theoretical foundation for the development of hydrogen leak detection technologies, risk assessment methodologies, and inherently safe system designs.

DECLARATION OF GENERATIVE AI AND AI-ASSISTED TECHNOLOGIES IN THE WRITING PROCESS

During the preparation of this work the author(s) used ChatGPT 5.0 in order to improve language and readability. After using this tool/service, the author(s) reviewed and edited the content as needed and take(s) full responsibility for the content of the publication.

REFERENCES

1. Yang X., Nielsen C.P., Song S., et al. (2022). Breaking the hard-to-abate bottleneck in china's path to carbon neutrality with clean hydrogen. *Nat. Energy* 7:955–965. DOI:10.1038/s41560-022-01114-6
2. Zhang M., Guan J., Tu Y., et al. (2021). Highly efficient conversion of surplus electricity to hydrogen energy via polysulfides redox. *Innovation* 2:100144. DOI:10.1016/j.xinn.2021.100144
3. Davis S.J., Lewis N.S., Matthew S., et al. (2018). Net-zero emissions energy systems. *Science* 360:eaas9793. DOI:10.1126/science.aas9793
4. Ueckerdt F., Bauer C., Dirnaichner A., et al. (2021). Potential and risks of hydrogen-based e-fuels in climate change mitigation. *Nat. Clim. Chang.* 2:384–393. DOI:10.1038/s41558-021-01032-7
5. IEA (2024). Global hydrogen review 2024. *IEA paris.*
6. Odenweller A., Ueckerdt F., Nemet G.F., et al. (2022). Probabilistic feasibility space of scaling up green hydrogen supply. *Nat. Energy* 7:854–865. DOI:10.1038/s41560-022-01097-4
7. Li J., Liu J., Dai H., et al. (2024). Rapid development of hydrogen in the energy sector raises safety regulatory concerns. *Innov. Energy* 2:100037. DOI:10.59717/j.xinn-energy.2024.100037
8. Li H., Cao X., Liu Y., et al. (2022). Safety of hydrogen storage and transportation: an overview on mechanisms, techniques, and challenges. *Energy Rep.* 8:6258–6269. DOI:10.1016/j.egyr.2022.04.067
9. European commission. HIAD 2.1, the hydrogen incident and accidents database.
10. Shu Z., Liang W., Zheng X., et al. (2021). Dispersion characteristics of hydrogen leakage: comparing the prediction model with the experiment. *Energy* 236:121420. DOI:10.1016/j.energy.2021.121420
11. H2tools. lessons learned, hydrogen tools.
12. Li J., Liu J., Wang T., et al. (2024). Analysis of the evolution characteristics of hydrogen leakage and diffusion in a temperature stratified environment. *Energy* 293:130598. DOI:10.1016/j.energy.2024.130598
13. Glenk G. and Reichelstein S. (2019). Economics of converting renewable power to hydrogen. *Nat. Energy* 4:216–222. DOI:10.1038/s41560-019-0326-1
14. Liang Q., Huang Y., Guo Y., et al. (2024). Efficient osmosis-powered production of green hydrogen. *Nat. Sustain.* 7:628–639. DOI:10.1038/s41893-024-01317-7
15. de Kleijne K., Huijbregts M., Knobloch F., et al. (2024). Worldwide greenhouse gas emissions of green hydrogen production and transport. *Nat. Energy* 9:1139–1152. DOI:10.1038/s41560-024-01563-1
16. Jiang X., Xu C., Yang Z., et al. (2024). Equivalent notional nozzle model for high nozzle pressure ratio leakage of petrochemical high-pressure facility. *Energy* 295:131027. DOI:10.1016/j.energy.2024.131027
17. Ra Y., Won H., Purushothaman A.K., et al. (2025). Numerical simulation of hollow-cone hydrogen underexpanded jet injection using a phenomenological barrel shock model. *Fuel* 390:134718. DOI:10.1016/j.fuel.2025.134718
18. Sun X., Lv J., Han Y., et al. (2025). A global evolution of the downward jet flame behavior: from the laminar to the turbulent. *Combust. Flame* 272:113906. DOI:10.1016/j.combustflame.2024.113906
19. Zhang G., Zhang Y., Shi P., et al. (2025). Near-field jet characteristics of a single-hole medium-/low-pressure hydrogen injector. *Energy* 314:134122. DOI:10.1016/j.energy.

2024.134122
20. Jeon D.S., Hwang G.J., Kim N.I. (2024). Lift-off characteristics of non-premixed jet flames of CH4 and cracked NH3 mixtures in laminar/turbulent transition. *Combust. Flame* 265:113462. DOI:10.1016/j.combustflame.2024.113462
21. Oh J. and Yoon Y. (2012). Liftoff height behavior in a non-premixed turbulent hydrogen jet with coaxial air. *Fuel* 91:134–140. DOI:10.1016/j.fuel.2011.08.008
22. Takahashi F., Mizomoto M. and Ikai S. (1982). Transition from laminar to turbulent free jet diffusion flames. *Combust. Flame* 48:85–95. DOI:10.1016/0010-2180(82)90117-1
23. Hwang G.J., Jeon D.S. and Kim N.I. (2023). Stabilization criteria of laminar lifted propane flames and their transition to turbulent lifted flames under extended pressures. *Fuel* 343:127960. DOI:10.1016/j.fuel.2023.127960
24. Tang Z., Wang Z. and Zhao K. (2023). Flame stabilization characteristics of turbulent hydrogen jet flame diluted by nitrogen. *Energy* 283:129100. DOI:10.1016/j.energy.2023.129100
25. Guo X., Li T. and Huang S., et al. (2025). Characteristics of ignition, combustion and emission formation of premixed ammonia-hydrogen blends by hydrogen-fueled pre-chamber turbulent jets. *Energy* 322:135573. DOI:10.1016/j.energy.2025.135573
26. Gomez-Lendinez D., Coenen W. and Sevilla A. (2024). Direct numerical simulation of the global transition in laminar low-density axisymmetric jets. *Int. J. Heat Mass Transf.* 229:125651. DOI:10.1016/j.ijheatmasstransfer.2024.125651
27. Shu Z., Lei G., Liu Z., et al. (2022). Motion trajectory prediction model of hydrogen leak and diffusion in a stable thermally-stratified environment. *Int. J. Hydrog. Energy* 47:2040–2049. DOI:10.1016/j.ijhydene.2021.10.103
28. Lyu S., Huang X., Peng S., et al. (2024). A novel method for analyzing the leakage and diffusion of hydrogen: first arrival time distribution. *Renew. Sust. Energ. Rev.* 198:114451. DOI:10.1016/j.rser.2024.114451
29. Li Y., Wang Z., Shang Z., et al. (2024). The investigation of hydrogen released on the mixed jets with an axisymmetric jet and an asymmetric jet. *Int. J. Hydrog. Energy* 49:1108–1125. DOI:10.1016/j.ijhydene.2023.07.092
30. Li D., Wen Y., Liu Y.C., et al. (2024). On the transition modes and mechanisms for laminar to turbulent lifted jet diffusion flames at normal- and micro-gravity. *Combust. Flame* 260:113269. DOI:10.1016/j.combustflame.2023.113269
31. Kang Y., Ma S., Song B., et al. (2024). Study on the hydrogen leakage diffusion behavior by obstacles in confined spaces. *Fuel* 358:130110. DOI:10.1016/j.fuel.2023.130110
32. Nugroho F.A.A., Bai P., Darmadi I., et al. (2022). Inverse designed plasmonic metasurface with parts per billion optical hydrogen detection. *Nat. Commun.* 13:5737. DOI:10.1038/s41467-022-33466-8
33. Yao N., Lin W., Shi L., et al. (2025). Experimental study on the operating state of high-power vehicular fuel cell system hydrogen supply subsystem with an in-situ ultrasonic-based gas component monitoring equipment. *Appl. Energy* 388:125699. DOI:10.1016/j.apenergy.2025.125699
34. Gong L., Yang S., Han Y., et al. (2022). Experimental investigation on the dispersion characteristics and concentration distribution of unignited low-temperature hydrogen release. *Process Saf. Environ. Protect.* 160:676–682. DOI:10.1016/j.psep.2022.02.055
35. Li J., Tian Z., Yang Q., et al. (2023). A new visual approach with the concentration calibration method for the hydrogen leakage and distribution research. *Fuel* 346:128132. DOI:10.1016/j.fuel.2023.128132
36. George W.K. (1989). The self-preservation of turbulent flows and its relation to initial conditions and coherent structures. *Adv. Turb.* 3973.
37. Pope S.B. (2000). Free shear flows (chapter 5) - turbulent flows (Cambridge University Press).

FUNDING AND ACKNOWLEDGMENTS

This work is supported by National Natural Science Foundation of China with No. 52322707. Academic Papers of the 28th Annual Meeting of the China Association for Science and Technology.

AUTHOR CONTRIBUTIONS

Luqiao Yao: Conceptualization, Methodology, Writing - original draft, Writing - review & editing. Jianwei Li: Funding acquisition, Project administration, Supervision, Writing - review & editing. Qingqing Yang: Resources, Validation, Visualization, Writing - review & editing. Zhonghao Tian: Data curation, Investigation, Software, Writing - review & editing. All authors contributed to and approved the final version of the manuscript.

DECLARATION OF INTERESTS

The authors declare no competing interests.

DATA AND CODE AVAILABILITY

The data that support the findings of this work are available from the corresponding author upon reasonable request.

SUPPLEMENTAL INFORMATION

It can be found online at: https://doi.org/10.59717/j.xinn-energy.2026.100148